Effective Notch Stress Approach-Based Fatigue Evaluation of Rib-to-Deck Welds Including Pavement Surfacing Effects

Qiudong Wang[1] · Bohai Ji[1] · Zhongqiu Fu[1] · Yue Yao[1]

Abstract

The effective notch stress-based fatigue evaluation approach considering the effect of pavement surfacing is developed and verified in this research. Firstly, the sensitivity of stresses at fatigable welds to pavement surfacing was investigated. It turns out that rib-to-deck weld is most sensitive to pavement surfacing. Secondly, the influence of pavement surfacing on initial cracking position of rib-to-deck weld was analysed. Subsequently, the relationship between notch stress and temperature was developed based on the numerical results, so is the relationship between initial cracking position and temperature. Finally, the fatigue damages evaluated by effective notch stress approach and traditional approach were compared and analysed. The results show that the stress dispersal behaviour through pavement surfacing further improves the fatigue durability of rib-to-deck welds. The initial cracking position is related to the pavement temperature, rather than the transverse loading positions of vehicle loads. The effective notch stress concentration position varies with the pavement temperature. Such variation should be reasonably considered in fatigue damage evaluation process where effective notch stress approach is applied.

Keywords Orthotropic steel decks · Pavement surfacing · Effective notch stress approach · Stress concentration · Fatigue damage

1 Introduction

Orthotropic steel decks (OSDs) have been widely used in medium- and long-span steel bridges because of their light weight, high strength, excellent wind-resistance, stability, and other advantages. However, the structural components are subjected to fatigue cracking under cyclic traffic loads due to the welding residual stress, local stress concentration, short stress influence lines, etc. (Liu et al. 2015; Xiao et al. 2008). Fatigue cracks have been detected in many steel bridges in the USA, China, Japan, and other countries (Yan et al. 2016). A survey conducted in 2006 revealed that 90.5% of fatigue cracks were located in OSDs on the Hanshin Expressway and Shuto Expressway in Japan. The crack propagation greatly threatens the structural safety and durability. Both coating deterioration and corrosion will be subsequently generated once the fatigue crack penetrates the deck plate, which will further accelerate crack propagation (Kainuma et al. 2016).

There are mainly four types of fatigue cracks in OSDs as shown in Fig. 1: (a) initiated at the rib-to-deck welds, labelled Type I; (b) initiated at the butt welds, labelled Type II (Xiao et al. 2005); (c) initiated at the diaphragm-to-rib welds, labelled Type III; and (d) initiated at the arc-shaped notch, labelled Type IV (Yan et al. 2016). Furthermore, Type I crack could be further divided into four types (see Fig. 2): toe-deck crack, root-deck crack, root-weld crack and toe-rib crack. In Fig. 1, Type I and III cracks are imaged by the authors in a suspension bridge located in Jiangsu, China. It can be seen that it has required drilled stop-holes to retard its propagation.

Much research has been conducted to investigate the fatigue performance of OSDs, as well as its influencing factors. Many welded specimens were tested to evaluate the fatigue durability of rib-to-deck welds (Ya et al. 2011; Fu

✉ Bohai Ji
  bhji@hhu.edu.cn

  Qiudong Wang
  hhuqdwang@hhu.edu.cn

  Zhongqiu Fu
  fuzhongqiu@hhu.edu.cn

  Yue Yao
  hhuyaoyue@hhu.edu.cn

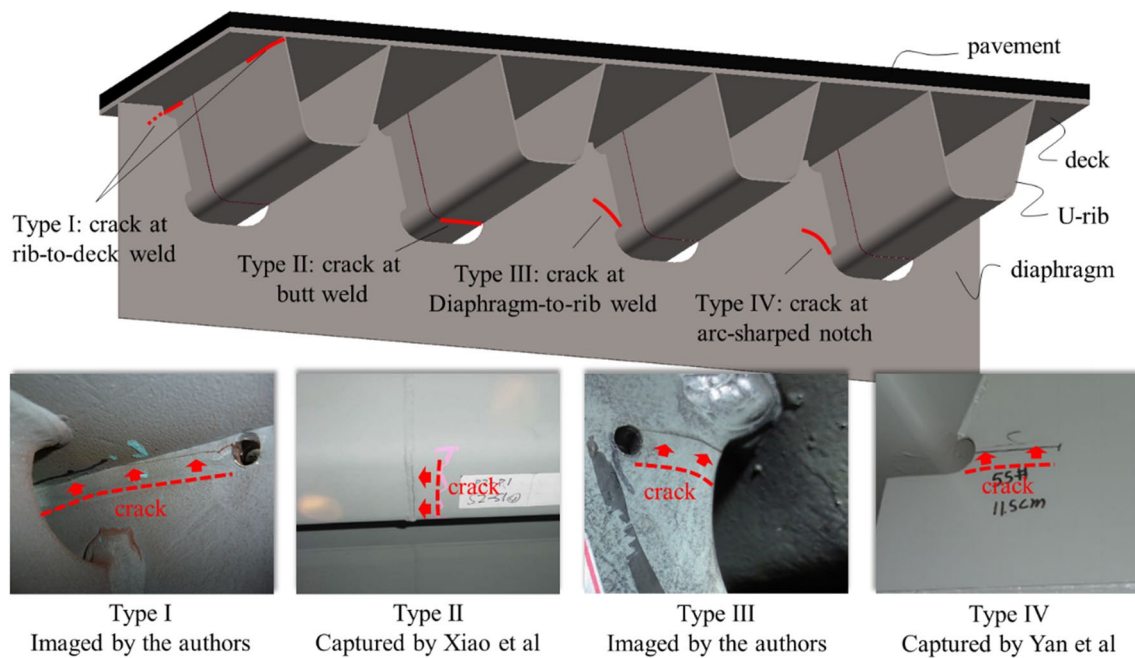[1] College of Civil and Transportation Engineering, Hohai University, No. 1 Xikang Road, Nanjing 210098, China
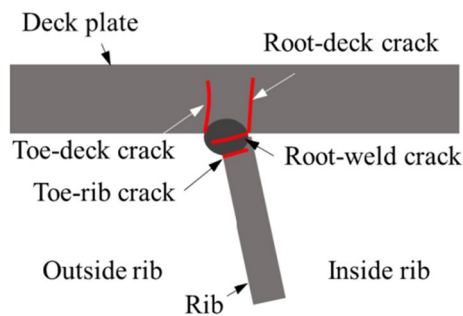
Fig. 1 Typical fatigue cracks in OSDs

Fig. 2 Fatigue cracks in rib-to-deck weld

et al. 2017a), diaphragm-to-rib welds (Zhang et al. 2015; Choi and Kim 2008), etc. The relative crack propagating pattern and fatigue strength were also analysed. However, most of tested specimens are pure steel components. In these tests, only welding residual stress, load amplitudes, and structural factors (e.g. the thickness of the deck plate) could be considered. The finite element methods are commonly adopted to investigate the fatigue performance of OSDs, as well as the effect of pavement surfacing (Li et al. 2014; Dong et al. 2013; Liu et al. 2016a, b). Most studies focused on the effect of pavement stiffness on the mechanical properties of OSDs. It turns out that the pavement surfacing improves the fatigue life of fatigable welds due to its composite stiffness (Li et al. 2014, 2016; Ji et al. 2013; Guo et al. 2008). In addition, the effect of road roughness of pavement on the fatigue performance of OSDs was also investigated (Cui et al. 2018). The stress dispersal behaviour (SDB) throughout the pavement

was also focused recently (Li et al. 2014; Cui et al. 2018). Current studies reveal that the dispersed wheel load tend to concentrate above the weld rather than distributing uniformly. However, to the best knowledge of the authors, some issues regarding the influencing mechanism of the stress dispersal behaviour remain unclear.

In addition, most studies were with a view to the effect of pavement surfacing on the fatigue life of welds in OSDs, as it was for the aforementioned research. However, since the pavement surfacing is sensitive to ambient temperatures, the effect of pavement surfacing on initial crack propagation path (i.e. propagation path right after crack initiation) remains unclear. The effective notch stress method (Lazzarin and Livieri 2001; Hobbacher 2015), by introducing a fictitious rounding to the weld root, is demonstrated to be a precise way to predicting the initial crack propagation path (i.e. the propagation path right after crack initiation) (Wang et al. 2019). Hence, further research is needed to investigate such differences in crack propagation paths. Furthermore, the effective notch stress approach is mostly applied to the evaluation of small components (Oh et al. 2014; Pedersen et al. 2010). The feasibility of the approach to the welds in OSDs still needs further research, especially when considering the combined effect of pavement surfacing and ambient temperatures.

Moreover, since the ambient temperatures are to be considered in this study, the effects of temperature on fatigue performance of welds in OSDs are discussed. Recently, most studies regarding the temperature effect on steel structures are focused on fire (Rahnavard and Thomas 2018, 2019;

Kloos and Wall 2019), high-temperature pavement paving (Liu et al. 2016a, b), post weld heat treatment (Aung and Hirohata 2019), etc. Due to the effect of fire, the steel component will be subjected to extremely high temperature (e.g. 1000 °C). However, such temperature cannot be reached in atmospheric conditions. The post weld heat treatment has considerable effect on the welding residual stress. However, the treatment doesn't work until the temperature exceeds a certain value (e.g. 400 °C). It is obvious that the ambient temperature has no influence on the welding residual stress at welds. During the process of high-temperature pavement paving, the temperature usually remains no more than 250 °C (Liu et al. 2016a, b). Therefore, the effect of high-temperature pavement paving on the fatigue performance of welds in OSDs could also be neglected. Relative studies show that very low temperatures (e.g. − 100 °C to − 200 °C) or very high temperatures (e.g. 300 °C to 400 °C) will influence the crack initiation and propagation (Guo et al. 2008). Considering that the temperatures in this study vary from − 10 °C to 70 °C, the temperature effect on steel components is neglected. However, since the asphalt pavement is sensitive to temperatures, the temperature effect on the mechanical properties of asphalt pavement is considered in this study.

The objectives of the present study consist of (1) determining the fatigue weld in OSDs most sensitive to pavement surfacing; (2) comprehensively investigating the effect of pavement surfacing on initial crack propagation path using effective notch stress approach; and (3) demonstrating the feasibility of application of effective notch stress approach to the fatigue evaluation of welds in OSDs, including the composite effect of pavement surfacing.

To accomplish the objectives mentioned above, the finite element analysis was performed to investigate the characteristics of stress dispersal behaviour through pavement surfacing. The fatigable welds most easily affected by the pavement surfacing were also analysed. Based on the analysis results, the effective notch-based sub-model was developed to investigate the effect of pavement surfacing on initial crack propagation path at rib-to-deck weld. The effective notch stress-based evaluation procedure was developed to involving the effect of pavement temperatures. The fatigue damages were assessed using both effective notch stress approach and traditional stress approach. The results were compared to demonstrate the feasibility of the proposed evaluation procedure.
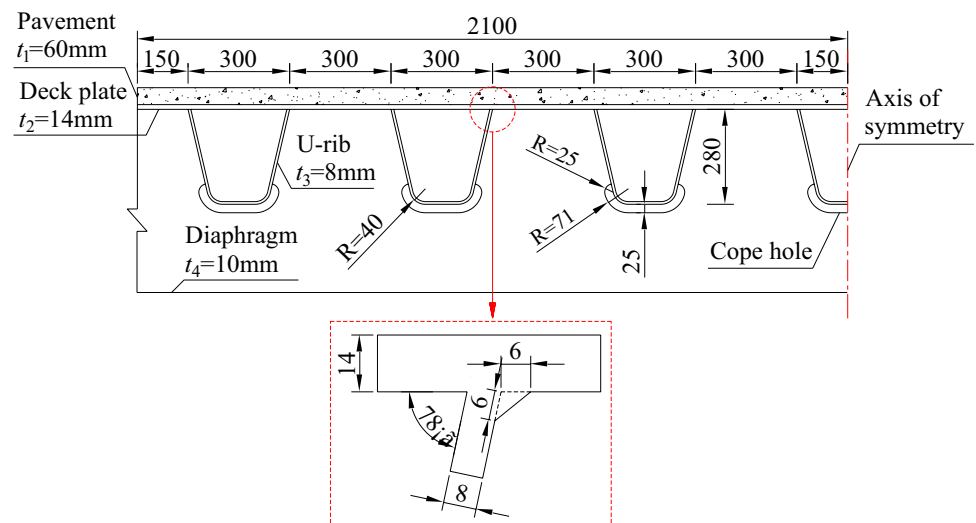
2 Stress Dispersal Behaviour

2.1 Analytical Model

To investigate the stress dispersal behaviour throughout the pavement surfacing, the finite element model (FEM) was developed using *ANSYS*. The OSD is simplified as being composed of seven U-ribs (labelled R1 to R7) and three diaphragms (labelled D1 to D3). The feasibility analysis of such simplification is as follows: (1) it has already been demonstrated that the FEM with seven U-ribs and five diaphragms could be used to simulate the stress characteristics of real structures with high accuracy (Fu et al. 2017b); and (2) according to the stress influence lines of OSDs, three diaphragms are precise enough for static analysis. In this model, the penetration rate of rib-to-deck weld was valued 100%. The dimensions of the FEM, including the geometric sizes of rib-to-deck weld, are marked in Fig. 3. The developed FEM is shown in Fig. 4. The cope holes closest to the rib-to-deck welds were not considered here.

Generally, it is suitable to simulate thin-walled structures using shell elements. However, the effects of weld

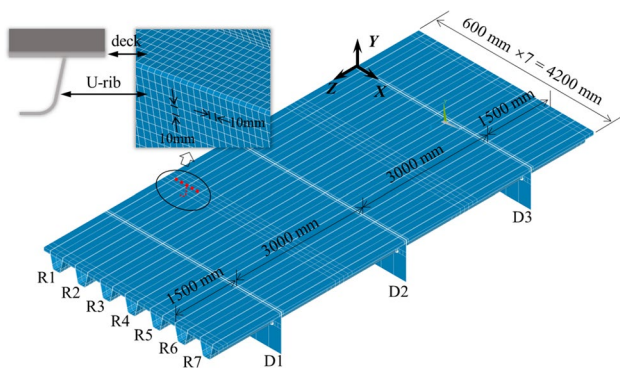Fig. 3 Dimensions of FE model (unit: mm)

Fig. 4 Schematic diagram of FE model

(a) Loading and boundary conditions

(b) Comparison of the stresses perpendicular to the weld

Fig. 5 Verification of the developed FE model

geometry cannot be precisely considered. In this study, the effective notch stress at weld root needs to be evaluated. Hence, the solid element is adopted instead of shell element. SOLID186-type elements were adopted to simulate both the OSD and asphalt pavement with a mesh size of 10 mm. This element is defined by 20 nodes having three degrees of freedom per node: translations in the nodal x, y, and z directions. The element supports plasticity, hyper elasticity, creep, stress stiffening, large deflection, and large strain capabilities. The meshing size is acceptable for the nominal stress analysis (Ji et al. 2013). The mesh size would be refined for notch stress analysis in the following sections.

Since the applied load in the FE analysis was small, all nodes at the bottom of the asphalt pavement were connected to the deck surface for simplicity. The Young's modulus of the deck and pavement are 210 GPa and 700 MPa respectively. The Poisson's ratios are both 0.3. As the stresses in this analysis were less than the yield strength of steel (e.g. 345 MPa for Q345qD-typed material), the linear finite element analysis was performed. The elasto-plastic strain-hardening relationship was not considered in this study. The failure mode of the used materials is not considered. The Chinese Standard "*Specifications for Design of Highway Steel Bridge*" was referred to for the double wheel load. The loading area was 600 mm (transverse) × 200 mm (longitudinal) (JGT D64 2015).

With respect to the boundary conditions, the displacement of the nodes on longitudinal end of the deck plate and U-sharped ribs were constrained to simulate the continuous deck plates and ribs in real bridges. The displacement of the nodes on the transverse end of the deck plate and diaphragms were also constrained. In addition, the displacement of the nodes at the bottom of the diaphragms was also constrained to simulate continuous diaphragms.
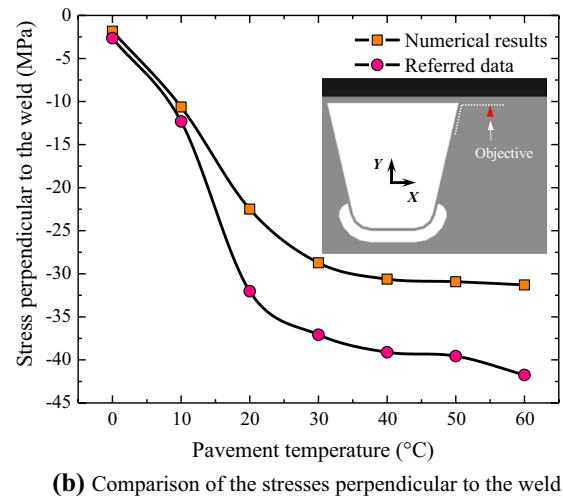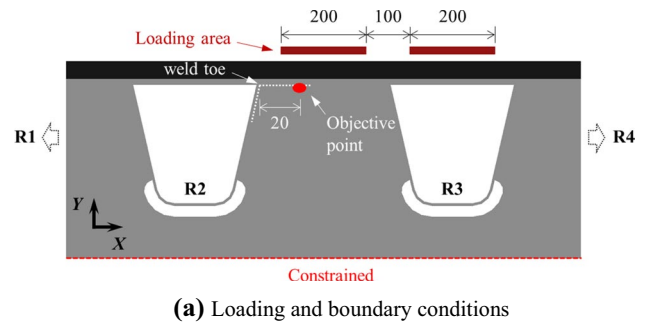
2.2 Verification of the Model

In order to verify the developed FE model, part of the test results (Li et al. 2016) were referred for comparison. To keep consistent with the specimen, another FE model was developed, of which the thickness of deck plate, U-rib and pavement was 12, 6 and 80 mm, respectively. The FE model was composed of 4 U-ribs, the same with the specimen. The loading case of S2-10 in the test was simulated, as shown in Fig. 5a. The loading magnitude was 50 kN, and the single loading area was 200 mm × 200 mm. It has been demonstrated that the stress 10 mm away from the weld is less affected by the weld geometry (Fu et al. 2017a). Hence, to eliminate the differences induced by weld geometry, the experimental data of strain gauge S2D10 (20 mm away from the weld toe) was referred. As the specimen was placed on the ground, the nodes at the bottom surface of diaphragms were constrained.

The elastic modulus of the pavement surfacing (E_P) is sensitive to the temperature. The relationship between E_P and pavement temperature (T) could be expressed by Eq. (1) (Liu et al. 2016a, b):

$$E_P = 11031 \times 10^{-0.01693 \cdot T} \tag{1}$$

The E_P at different temperatures are listed in Table 1. The E_P of the FE model will be set as different values according to Table 1 to represent the effect of pavement temperature. plate at rib intersection with diaphragm in

Both the numerical and referred test results are plotted in Fig. 5b. There exist some differences between the numerical and experimental results. However, the numerical results are similar to the experimental results at low temperatures. Additionally, the variation trend of the curves is similar. It demonstrates that the developed FE model is acceptable for the static analysis in this study.

2.3 Distribution of Dispersed Wheel Loads

The wheel load is assumed to be uniformly dispersed onto the deck plate surface with a certain dispersal angle in some specifications. However, it was found that the wheel load tended to be concentrated above the rib-to-deck welds. Since the elements for the pavement and deck plate were fully connected by sharing nodes at the interface, the stresses at the sharing nodes couldn't be directly regarded as the contact stresses. Considering that both pavement and deck plate were simulated by SOLID186 element with 20 nodes, the stresses at the nodes closet to the interface were regarded as the contact stress for simplification. A FE model involving the contact behaviour by adopting spring elements (typed Combine39) was also developed. The node stresses at and closet to the interface were compared. The results showed that the stress difference was within 8%, indicating that the simplification was acceptable.

Figure 6 shows the distribution of dispersed wheel load, where the effect of elastic modulus of pavement surfacing is considered. The numerical results demonstrate that the dispersed load tends to be concentrated above rib-to-deck welds, especially above the weld beneath the wheel load. The maximum value of dispersed load was 0.77 and 1.105 MPa when the elastic modulus of pavement surfacing was set as 720 and 11,031 MPa, respectively. It indicates the considerable effect of pavement temperatures on SDB. In addition, some dispersed loads adjacent to the wheel are with positive values. It indicates that tensile stress is generated at the interface between the pavement surfacing and deck plate. Even though the tensile stress is smaller than the pull-off strength of the bonding layer, the disengagement at the interface might be generated by cyclic heavy load application.
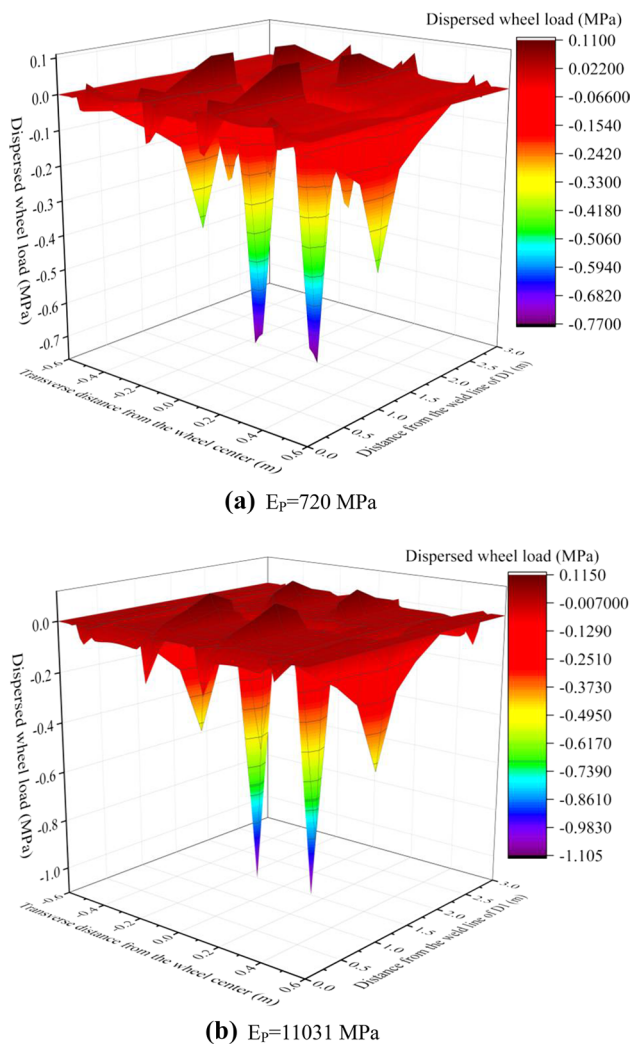

(a) E_P=720 MPa

(b) E_P=11031 MPa

Fig. 6 Distribution of dispersed wheel load

2.4 Effect of Temperatures on SDB

The distributions of dispersed wheel load at different temperatures are shown in Fig. 7. At low temperature, the dispersed wheel load tends to be concentrated above the rib-to-deck welds. At − 10 °C, the dispersed wheel load at the loading center exceeds 1.0 MPa, which is over twice the applied load (0.5 MPa). However, the dispersed wheel load above rib-to-deck welds decreases with increasing temperature. Additionally, the wheel load tends to be dispersed onto the deck surface between weld lines. It means that more adverse out-of-plane

Table 1 Elastic modulus of asphalt pavement at different temperatures

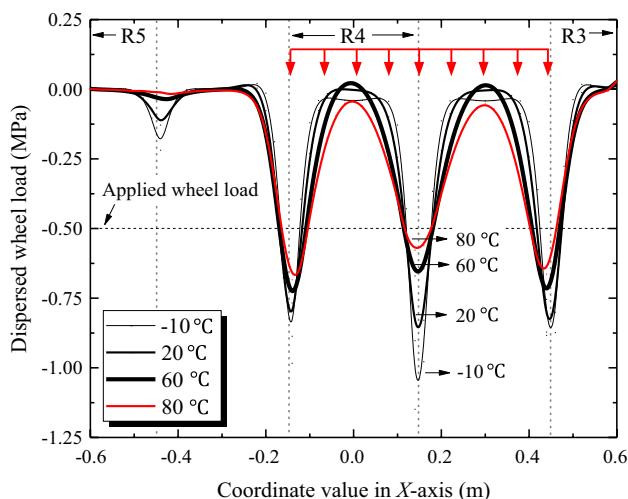| T (°C)	− 10	0	20	40	60	80
E_P (MPa)	16,290	11,031	5058	2320	1064	488

Fig. 7 Distribution of dispersed wheel load and its variation with temperature

deformation will be induced at higher temperatures due to the stress dispersal behaviour.

2.5 Effect of Local Stiffness on SDB

Figure 8 shows the distribution of dispersed wheel load while the wheel moves from the mid-span between D2 and D3 ($z = 1.5$ m) to the weld line above D2 ($z = 3.0$ m). The loading center kept to be aligned with the center of R4. When $z = 1.5$ m, the dispersed wheel load concentrates above the rib walls of R4 and adjacent rib walls. The maximum value of dispersed wheel load is equated to about 0.75 MPa, which is 1.5 times the applied wheel pressure.
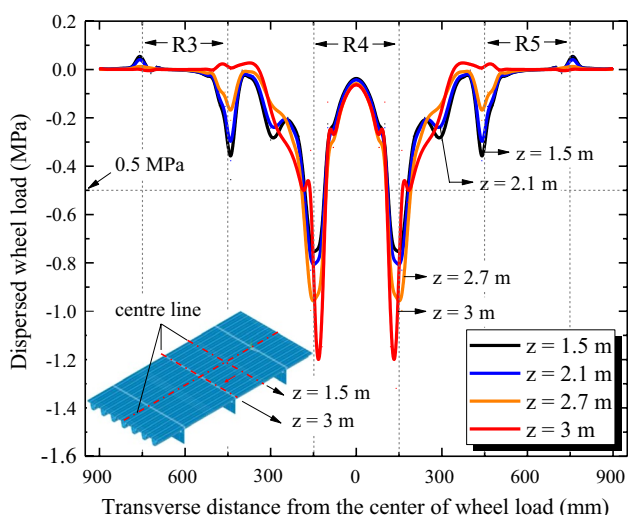
When the wheel load moves to the weld line of D2, the dispersed wheel load above the rib wall of R4 keeps increasing. When $z = 3.0$ m, the dispersed load above the rib wall of R4 increases to about 1.2 MPa. This indicates that the dispersal behaviour is related to the local stiffness of orthotropic steel decks.

The local stiffness of the OSD cannot be obtained directly from the solution, however, it could be represented by the reciprocal of the relative displacement. In this study, the node displacement at the interface was regarded as the displacement of the deck plate. Considering that the node displacement (Δ_y) was related to the local stiffness of orthotropic steel decks, the reciprocal of the displacement ($1/\Delta_y$) was adopted to represent the local stiffness. It was obvious that the greater the local stiffness was, the smaller the $1/\Delta_y$ was. Hence, the relationship between the maximum value of dispersed wheel load and $1/\Delta_y$ was plotted in Fig. 9. The abscissa was $1/\Delta_y$, and the ordinate was the maximum value of dispersed wheel load concentrated above the rib wall of R4. A logarithmic function could be used to fit the data, indicating the logarithmic relationship between the maximum value of dispersed wheel load and the local stiffness of OSDs.

3 Fatigable Welds Affected by Pavement Surfacing

3.1 Loading Modes

Three loading modes (see Fig. 10) were applied to the model respectively: (1) mode I, the wheel load is applied at the surface of asphalt pavement; (2) mode II, the wheel load is
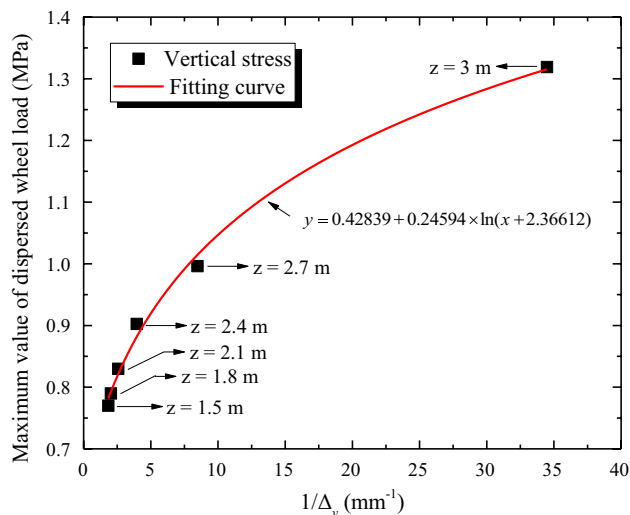

Fig. 8 Distribution of dispersed wheel loads at the surface of deck plate

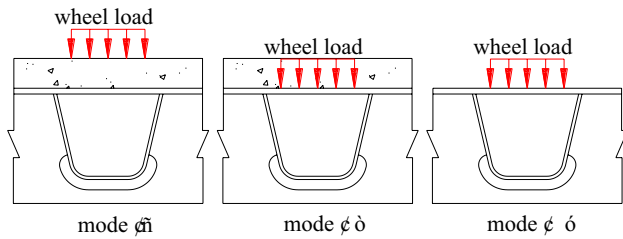**Fig. 9** Logarithmic relationship between the dispersed wheel load and local stiffness

Fig. 10 Three loading modes adopted in FE analysis

applied at the surface of deck plate; and (3) mode III, the asphalt pavement is not considered, and the wheel load is applied at the surface of deck plate. It is clear that the effects of pavement stiffness and the stress dispersal behaviour are involved in mode I, while none of them are included in mode III. With regard to mode II, only the effect of pavement stiffness is considered.

3.2 Fatigable Welds Affected by SDB

There are many types of fatigable welds in OSDs as mentioned before. The SDB might influence the fatigue performance of welds due to the dispersed load concentration above the welds. Hence, modes I, II, and III were applied to investigate the differences. Two loading positions were considered here: (1) at mid-span between diaphragms D2 and D3 ($z = 1.5$ m); (2) above the weld line of diaphragm D2 ($z = 3.0$ m). The number of each stress extracting position is illustrated in Fig. 11. For comparing, the relative value of the Von-Mises equivalent stress (S_{eqv}) was defined as the ratio of S_{eqv} in modes II and III to S_{eqv} in mode I, as plotted in Fig. 12.

Regarding P1 and P2, the relative value of mode II is decreased by 31% and 37%, respectively. It indicates that the stress concentration becomes more severe due to the
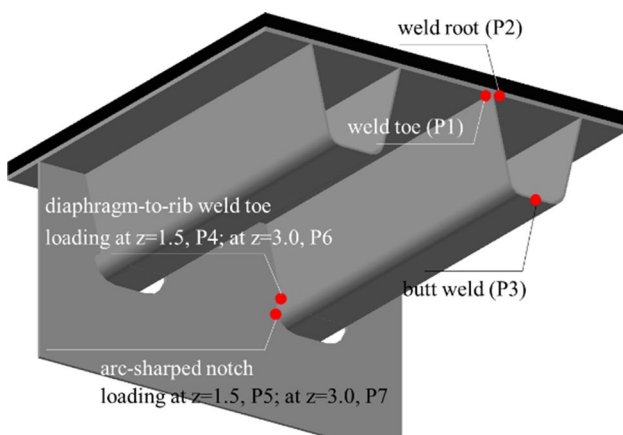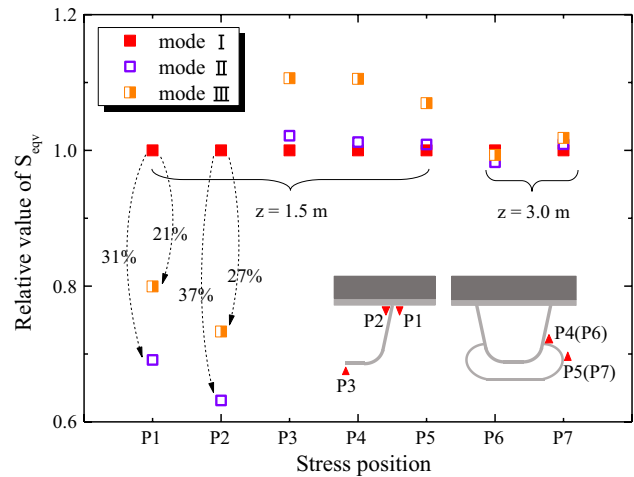

Fig. 12 Relative value of S_{eqv}

dispersal behaviour. This might be attributed to the fact that the dispersed wheel load tends to be distributed near the weld line of rib-to-deck weld when the asphalt pavement has a low elastic modulus (e.g. 700 MPa as used here) (Li et al. 2014). As discussed above, the SDB at high temperatures will lead to more adverse out-of-plane deformation around the weld. In addition, the relative value is 21% and 27% for mode III, indicating that the positive effect induced by the pavement stiffness is not obvious due to the adverse effect of stress dispersal behaviour. The relative value in mode III might be greater than 1.0 when the asphalt pavement has a higher elastic modulus.

For P3 to P7, the relative value in mode II almost overlaps that of the S_{eqv} in mode I. It suggests that the stress dispersal behaviour has no influence on the fatigue durability of butt welds, diaphragm-to-rib welds and the arc-shaped notch. The relative value in mode III is increased by nearly 10% for P3 to P5, demonstrating the positive influence of the pavement stiffness. The stresses at P6 and P7 remain almost unchanged regardless of loading mode. It might be attributed to the greater stiffness therewith.

Therefore, it could be concluded that both the pavement stiffness and the SDB exert a considerable influence on the fatigue durability of rib-to-deck welds. The influencing mechanism is to be discussed in the following sections.

4 Effect of Pavement Surfacing on Cracking Position

4.1 Effective Notch-Based Model

The rib-to-deck weld was focused here according to the former analysis. The stress at the weld root is more easily affected by the asphalt pavement. To investigate the stress

Fig. 11 Number of stress extracting positions

characteristics, a refined FE model was developed based on the sub-model method. The sub-model was composed of R4 and half of R3 and R5, as shown in Fig. 13. The rib-to-deck weld of R4 was selected as the objective weld, as before. For analyzing both the stress characteristics and initial crack initiation position at weld root, an effective notch, was arranged at the weld root. The radius of the notch was set as 1 mm. The elements around the notch

Fig. 13 Refined sub-model with the effective notch at weld root

were equally divided into 24 parts (Hobbacher 2015), where the refined mesh size was nearly 0.2 mm. The previous study has demonstrated that the meshing size is acceptable for notch stress analysis (Wang et al. 2019).

4.2 Influence of Transverse Loading Positions

To investigate the effect of transverse loading positions on rib-to-deck weld, the transverse distribution model was adopted (Fig. 14a). Figure 14b–f shows the effective notch stress at each loading position. There is a stress concentration spot at the edge of the root notch. The maximum stress appears when the center of the wheel load is 0.1 m left of the objective weld line (Fig. 14e). In addition, the stress concentration position remains unchanged when the transverse loading position changes. It indicates that the crack initiation position is independent of transverse loading position. In these cases, fatigue cracks might be generated at the upper side of the effective notch under cyclic traffic loads. This may correlate with the root-deck crack in OSDs (Fig. 15), as detected in real steel bridges.
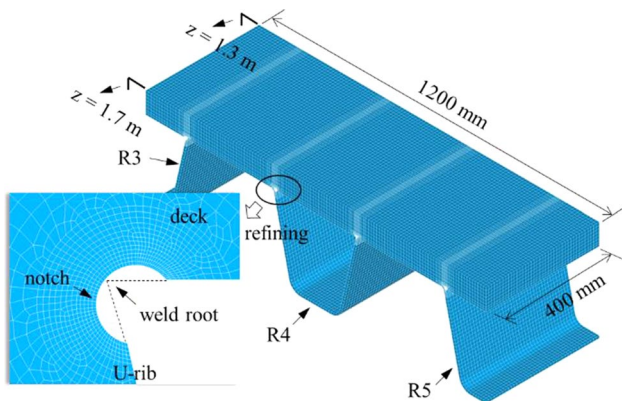

(a) Transverse distribution of the wheel load

(b) Above the weld line

(c) 0.1 m right of the weld line

(d) 0.2 m right of the weld line

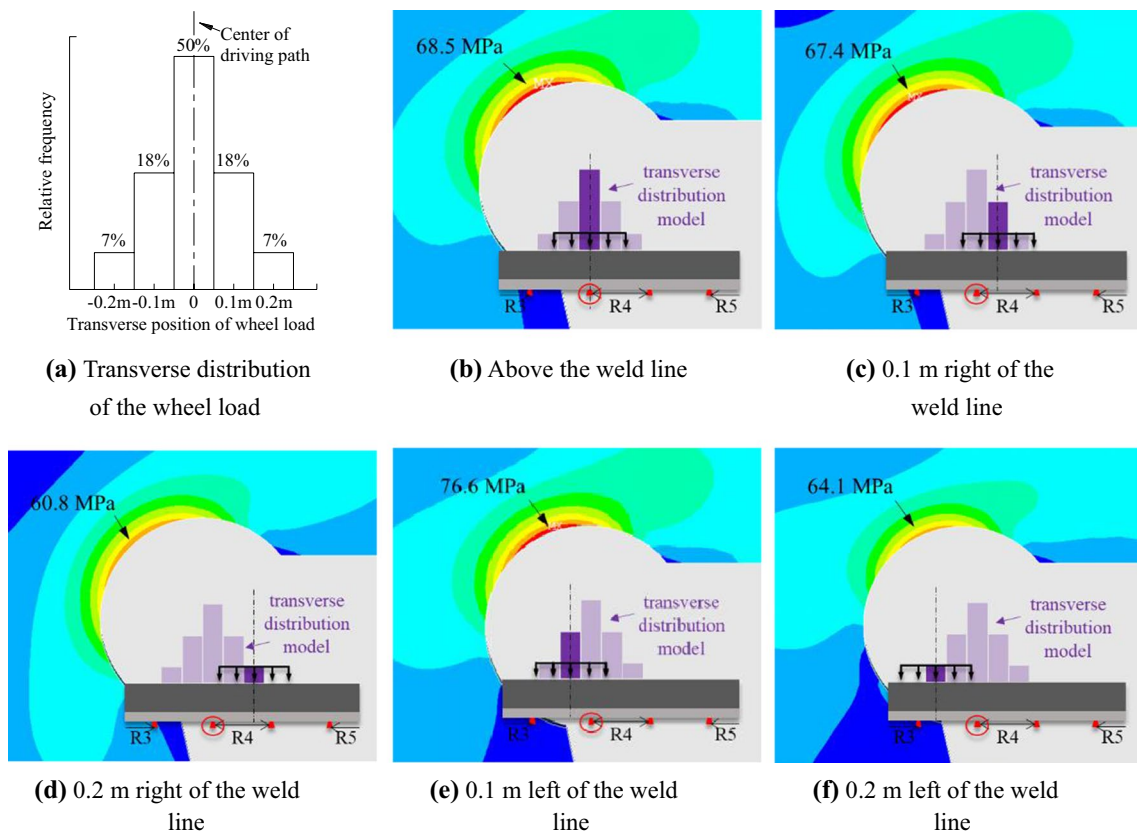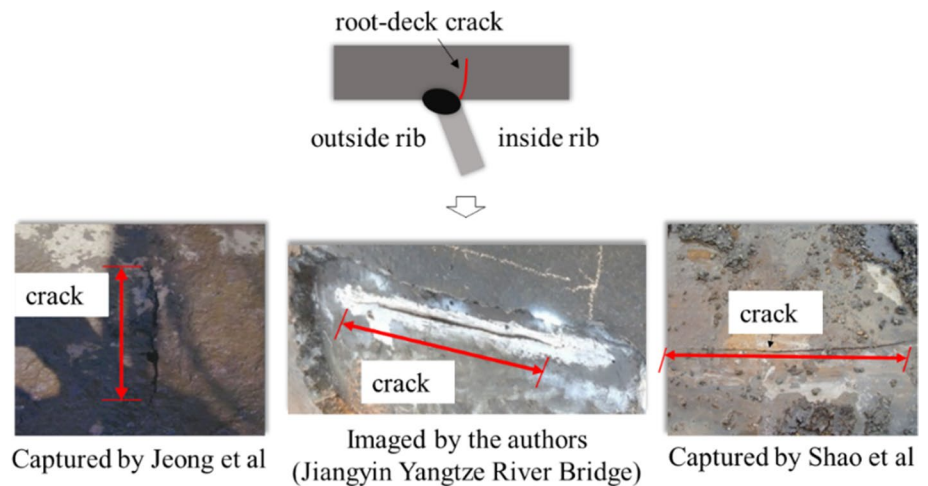**(e)** 0.1 m left of the weld line

(f) 0.2 m left of the weld line

Fig. 14 Distribution of effective notch stress at different transverse loading positions

Fig. 15 Root-deck cracks in OSDs

Captured by Jeong et al

Imaged by the authors
(Jiangyin Yangtze River Bridge)

Captured by Shao et al

4.3 Influence of Pavement Temperatures

4.3.1 Comparison of Out-of-Plane Deformation

The stress nephogram at − 10 °C and 80 °C are shown in Fig. 16, where the effect of stress dispersal behaviour is considered. Considering that the deformation is greater at higher temperatures, the deformation factor for 80 °C is set to 800 while it is set to 2000 at − 10 °C. The angle of the deformed geometric profile at the weld toe and weld root was calculated to evaluate the deformation. At − 10 °C, the angle at weld root decreases when eliminating the effect of stress dispersal behaviour (Fig. 16a). This means that the SDB at low temperatures can help to reduce the stress concentration at weld root. However, the out-of-plane deformation increases at 80 °C when considering the effect of SDB (Fig. 16b). It demonstrates that more adverse out-of-plane deformation will be induced at high temperatures due to SDB. The deformation at weld toe is less affected by the stress dispersal behaviour, especially at low temperatures.

Fig. 16 Comparison of out-of-plane deformation at different temperatures
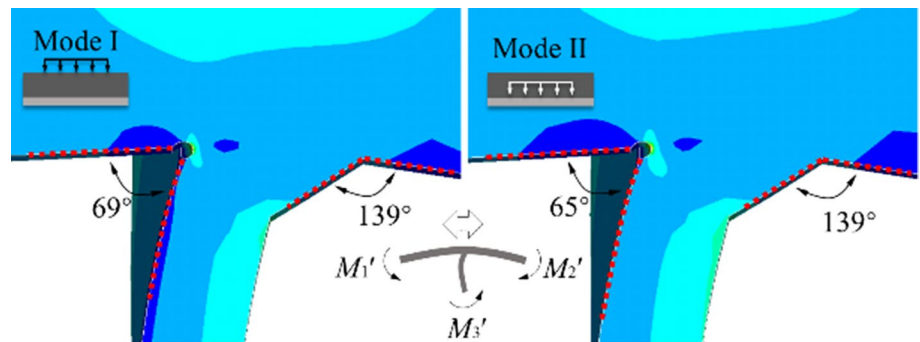
(a) at -10 °C (deformation factor: 2000)
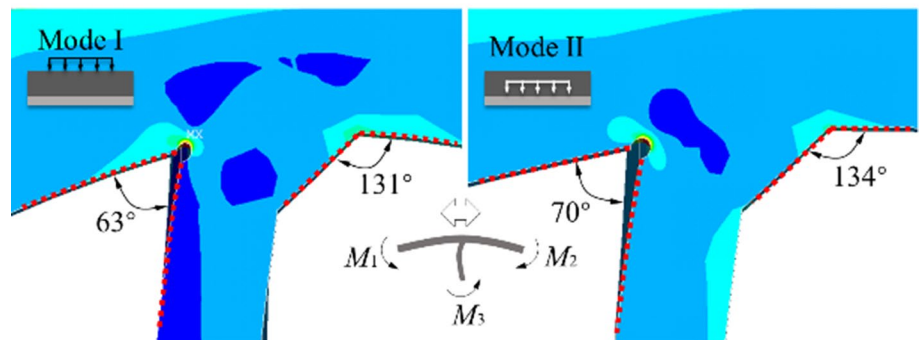
(b) at 80 °C (deformation factor: 800)

4.3.2 Comparison of Cracking Position

The nephogram of effective notch stress at − 10 °C and 80 °C are shown in Fig. 17. At − 10 °C, the maximum effective notch stress is 21.2 MPa in Mode I, while it increases to 26.4 MPa in Mode II. However, the effective notch stress varies from 80 MPa (Mode I) to 48 MPa (Mode II) at 80 °C, which shows the opposite trend. This could be attributed to the fact that more adverse out-of-plane deformation was induced at high temperatures due to the stress dispersal behaviour.

4.3.3 Variation of Effective Notch Stress

Figure 18 shows plots of the numerical results at different temperatures. The exponential function expressed by Eq. (2) was adopted to fit the results in Mode I, while the linear function expressed by Eq. (3) was used to fit the results in Mode II. It reveals that the effect of SDB on notch stress is non-linear, while it is linear for the effect of elastic modulus. In addition, there is an intersection point between these two fitting curves, at about 40 °C. It is believed that the SDB has no effect on the stress concentration at 40 °C, and the relative value of effect notch stress is 1.0 threat. Both Eqs. (2)
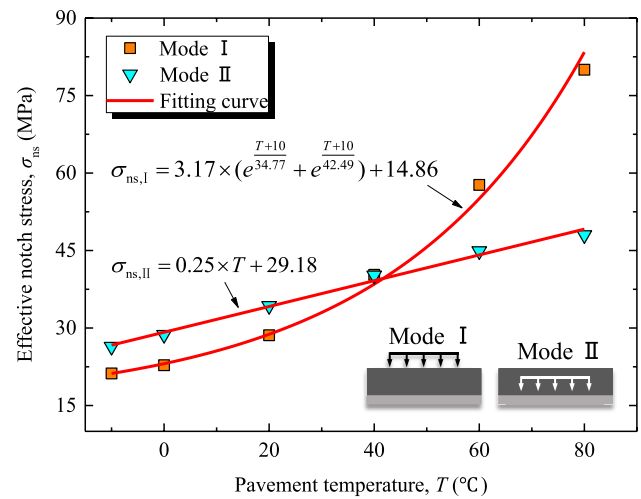

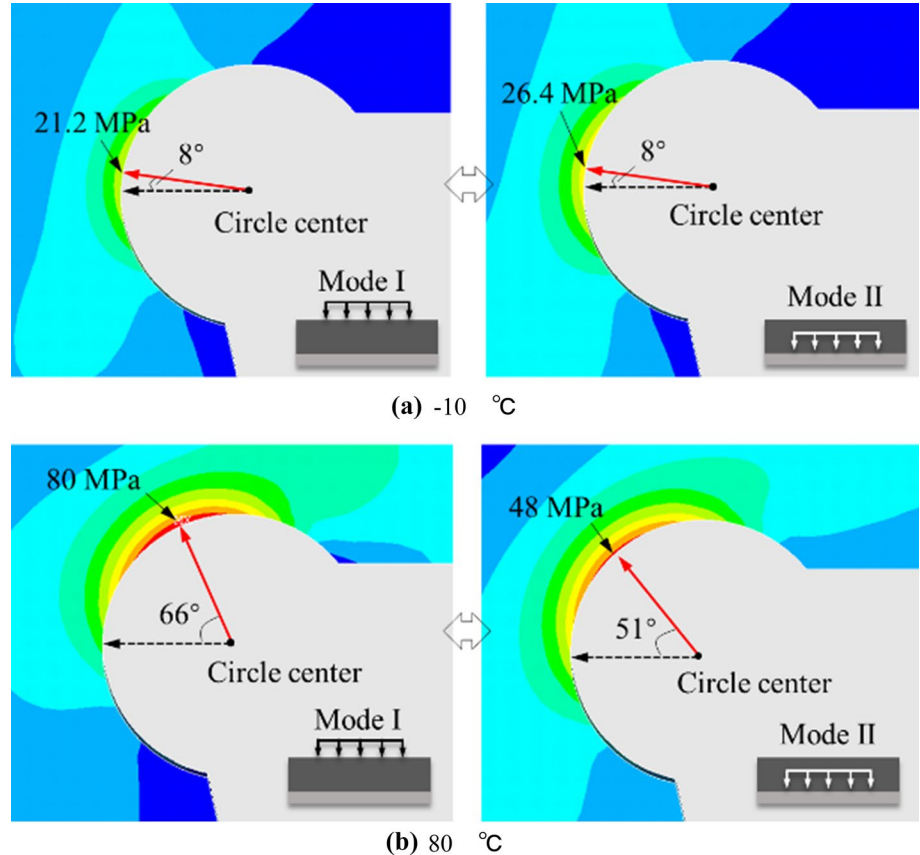**Fig. 18** Effective notch stress at different temperatures

and (3) are to be adopted in the fatigue damage evaluation in Sect. 5.

$$\sigma_{ns,I} = 3.17 \times \left(e^{\frac{T+10}{34.77}} + e^{\frac{T+10}{42.49}} \right) + 14.86 \tag{2}$$

$$\sigma_{ns,II} = 0.25 \times T + 29.18 \tag{3}$$

Fig. 17 Concentration of effective notch stress at different temperatures
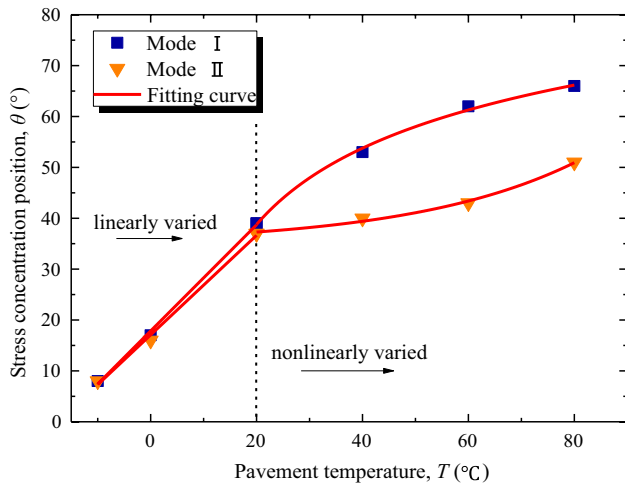

(a) -10 ℃

(b) 80 ℃

Fig. 19 Stress concentration position at different temperatures

where $\sigma_{ns, I}$ and $\sigma_{ns, II}$ is the effective notch stress in Mode I and II, respectively.

The stress concentration position also changes with the temperature. The angle in polar coordinates (θ), as illustrated in Fig. 17, is adopted to represent the position. The angles at different temperatures are plotted in Fig. 19. The stress concentration position locates at the lower inclined side of the root notch at low temperatures (i.e., 0 °C). The angle (θ) in Mode I and II varies linearly when the pavement temperature (T) is less than 20 °C. While the pavement temperature (T) exceeds 20 °C, the angle (θ) in Mode I and II varies nonlinearly with T. In addition, the angle in Mode II is lower than that in Mode I when the temperature exceeds 20 °C, indicating the considerable influence induced by the SDB. The relationship between the angle (θ) and the pavement temperature (T) could be expressed by Eqs. (4) and (5), where θI and θII are the angle in Mode I and II, respectively. The Eqs. (4) and (5) are also to be adopted in the fatigue damage evaluation in Sect. 5.

$$\theta_I = \begin{cases} 1.04T + 17.86, & -10 \leq T < 20 \\ 72.02\ln(0.57\ln T), & 20 \leq T \leq 80 \end{cases} \quad (4)$$

$$\theta_{II} = \begin{cases} 0.98T + 17.07, & -10 \leq T < 20 \\ 1.26e^{0.032T} + 34.91, & 20 \leq T \leq 80 \end{cases} \quad (5)$$

5 Fatigue Damage Evaluation

5.1 Valuing of Stress Amplitude

As discussed above, the stress concentration position determined by effective notch varies with the pavement temperatures. As a result, the fatigue damage induced by vehicle loads no longer accumulates in the same position, which will affect

the estimated fatigue damage. However, the effective notch at weld root is virtual. Therefore, whether the variation of stress concentration position should be considered in fatigue damage evaluation needs to be further verified. For this purpose, the commonly used sub-model without the effective notch was developed. The refined meshing size was set as 1 mm. Considering that the effective notch was introduced at the weld root, the equivalent stress (σ_{seqv}) at weld root was adopted to evaluate the fatigue damage, subsequently to make a comparison with that evaluated by effective notch stress in the following analysis.

Due to the quantity of elements of effective notch-based sub-model, the computing process is time-consuming. Considering that the equivalent stress amplitude equals to the equivalent stress at critical loading position (see Fig. 20), the stress amplitude could be obtained without calculating the stress wave. Hence, the effective notch stress amplitudes were calculated by using Eqs. (2) and (3).

The equivalent stress (σ_{seqv}) at weld root varied with the pavement temperatures (T) is plotted in Fig. 21. The relationship between σ_{seqv} and T is similar with that between σ_{ns} and T: the σ_{seqv} in Mode I varies exponentially with T, while the σ_{seqv} in Mode II varies linearly with T. The exponential and linear relationship could be expressed by Eqs. (6) and (7) respectively, which will also be adopted for fatigue damage estimation.

$$\sigma_{seqv,I} = 6.48 \times e^{\frac{T}{57.94}} - 1.90 \quad (6)$$
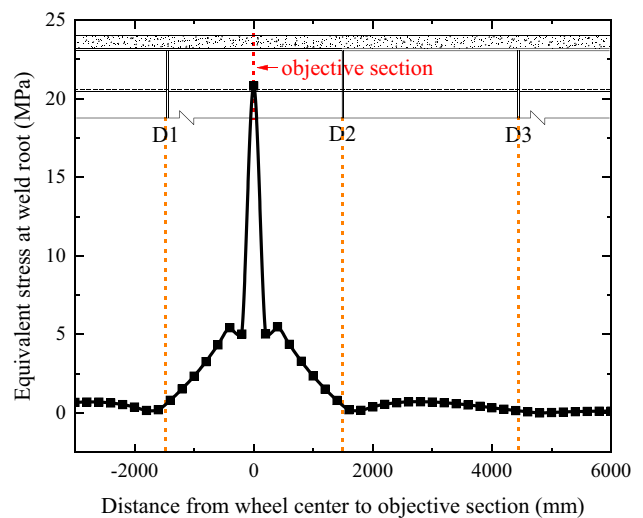
$$\sigma_{seqv,II} = 0.12 \times T + 5.55 \quad (7)$$

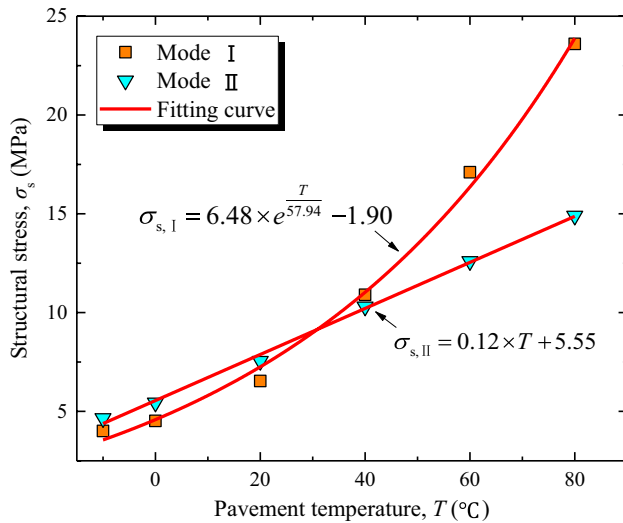**Fig. 20** Equivalent stress wave at weld root

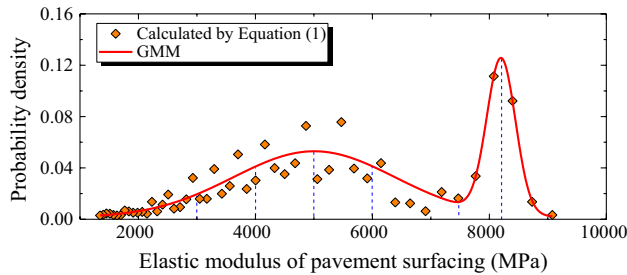**Fig. 21** Equivalent stress at weld root at different temperatures

Fig. 22 Probability density distribution of pavement modulus

5.2 Measured Data-Based Pavement Modulus

As illustrated above, both the pavement stiffness and SDB are sensitive to the temperature. Here, the field-measured data of pavement surfacing was referred (Liu et al. 2016a, b), and the relative modulus calculated by Eq. (1) was plotted in Fig. 22. A Gaussian model (GMM) was adopted to fit the data to a probability distribution. It is unpractical to calculate the fatigue damage using each data point. For simplicity, the fitted GMM curve is approximately divided into 8 parts according to observed inflection points. Then the average modulus of each part could be calculated by Eq. (8):

$$E_j = \frac{\sum_1^n E_i p_i}{\sum_1^n p_i} \tag{8}$$

where E_j is the average modulus of each part; E_i is the calculated data; and p_i is the relative probability density.

Then the probability density of E_j (labelled P_j) could be calculated by Eq. (9). The average modulus of each part, as well as the relative probability density, are given in Table 2. The relative average temperature (T_j) could then be obtained by using Eq. (1), which will be used to obtain the relative stress and angle by using Eqs. (2)–(7).

$$P_j = \sum_1^n p_i \tag{9}$$

5.3 Procedure of Fatigue Damage Evaluation

As stated above, the stress concentration position at introduced weld notch varies with the pavement temperatures. It means that the fatigue damage is not accumulated at the same position in a given year. It is obvious that whether the variation of stress concentration position is considered affects the estimated fatigue life. For this purpose, totally three types of fatigue damages were calculated: (1) using the effective notch stress and neglecting the variation of stress concentration position; (2) using the effective notch stress and considering the variation of stress concentration position; and (3) using the equivalent stress (σ_{seqv}) at weld root without notch.

Figure 23 shows the flowchart of the fatigue damage evaluation process. The effective notch stress (σ_{ns}) and the equivalent stress (σ_{seqv}) corresponding to the average temperature (T_j) could be calculated. It should be noted that this study aimed to investigate the feasibility of effective notch stress approach rather than predicting the fatigue damage of real-life bridges. Hence, the stress amplitude induced by single wheel load was adopted to make a comparison. The number of loading cycles from a single wheel was assumed to be 1000 per day here. The S–N curves of FAT 225 and FAT 90 recommended by IIW were adopted for effective notch stress and the equivalent stress analysis, respectively. Then the fatigue damage in a year could be calculated by using Eqs. (10) and (11):

$$N_j = \frac{2 \times 10^6 \times \Delta\sigma_R^m}{\Delta\sigma_j^m} \tag{10}$$

$$D = \sum_{j=1}^{8} \frac{n_j}{N_j} = \sum_{j=1}^{8} \frac{365 \times 10^3 \times P_j}{N_j} \tag{11}$$

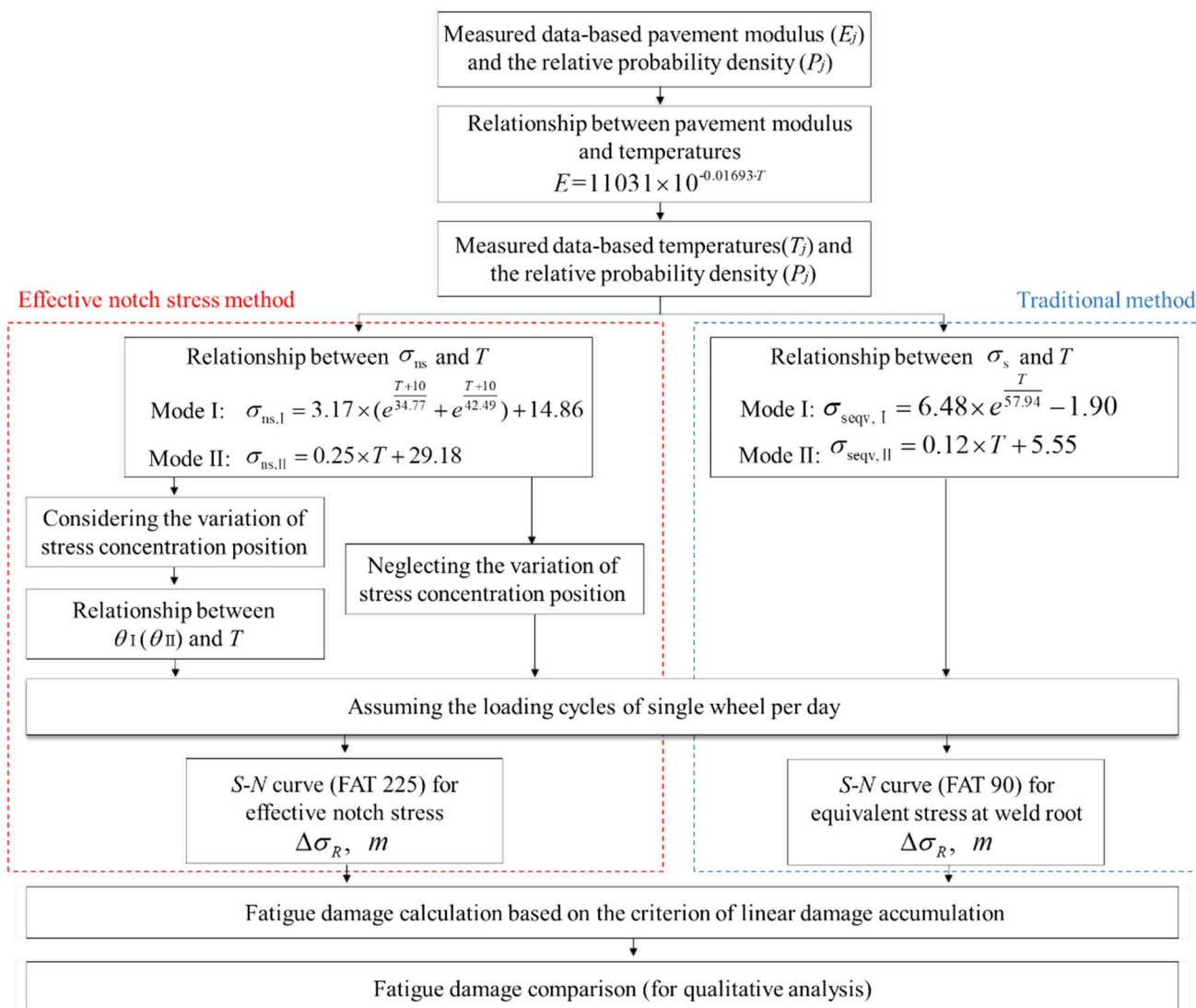| Table 2 Average elastic modulus of pavement								
E_j (MPa)	1722	2558	3573	4517	5460	6632	8000	8454
P_j	0.0412	0.08877	0.18509	0.18819	0.18808	0.11453	0.11111	0.08303

Fig. 23 Flowchart of the procedure of fatigue damage evaluation

where $\Delta\sigma_R$ is the fatigue strength recommended by IIW; $\Delta\sigma_j$ is the stress amplitude induced by a single wheel load; and m is the absolute value of the slope of the S–N curve.

5.4 Comparison of Fatigue Damage

As the measured data was reduced to eight typical values, eight stress concentration positions were obtained based on Eqs. (4) and (5). Figure 24 shows the calculated fatigue damages in a year. The fatigue damage accumulated at each stress concentration position is different from each other. Based on the measured data, the maximum fatigue damage in Mode I and II occurs at the position of 46.9° and 38.1°. Fatigue cracks will initiate at the position accumulated with maximum fatigue damage.

The fatigue damages calculated by different approaches were listed in Table 3. The fatigue damage considering the variation of stress concentration positions is close to the one calculated by the equivalent stress (σ_{seqv}) at weld root, while the fatigue damage neglecting the variation of stress concentration positions is unreasonable. It reveals that the differences in stress concentration position should be considered in the fatigue life evaluation when the effective notch stress approach is applied. In addition, the fatigue damage in Mode I is smaller than that in Mode II, demonstrating the positive effect of SDB on the fatigue durability of rib-to-deck welds.
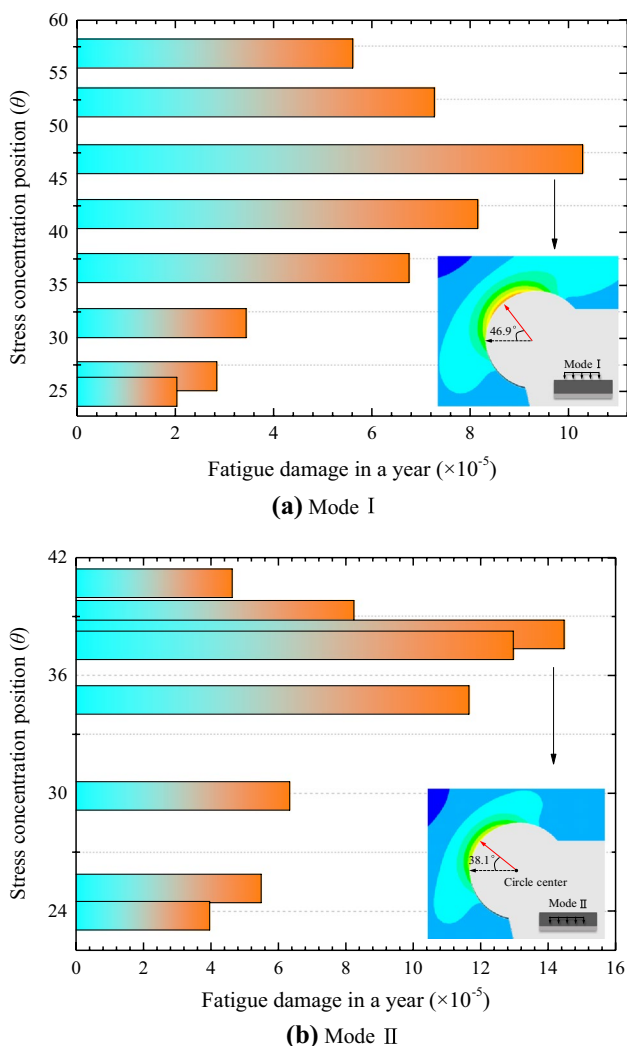
(a) Mode I

(b) Mode II

Fig. 24 Notch stress-based fatigue damage considering the variation of stress concentration position

6 Discussions

Overall, the research presented herein investigates the composite effect of the pavement surfacing on the fatigue performance of welds in OSDs. We found that the effective notch stress concentration position at weld root varies with the pavement temperatures. Then, we established the mathematic relation between the stress concentration position and the pavement temperature based on numerical results. The fatigue damage evaluated by the traditional method was also calculated for comparison. The results reveal that the differences in stress concentration position should be considered when applying the effective notch stress approach to fatigue life evaluation.

However, it should be noted that the variation of effective notch stress concentration position is induced by the variation of pavement temperatures. If the composite effect of pavement surfacing is neglected, the stress concentration region will remain unchanged. Then the procedure of fatigue damage evaluation will be the same with the nominal or hot-spot stress-based evaluating procedure.

Furthermore, fatigue test considering the combined effect of pavement surfacing and temperatures should be conducted to further demonstrate the proposed procedure of effective notch stress-based fatigue damage evaluation. To simulate the variation of pavement temperatures in real world bridges, dry ice and silicon rubber heater could be adopted to control the pavement temperatures of specimens. In addition, the fatigue damage in a given year distributes nonuniformly around the effective notch (see Fig. 24). If we take some fatigue preventative measures to control the stress concentration position (i.e. uniformly distributed in a given year), the fatigue life could be further extended. Therefore, the effective notch stress concentration position could be considered as one of the critical parameters in the validity assessment of proposed fatigue preventative measures in the future.

7 Conclusions

(1) The rib-to-deck weld is significantly affected by the stress dispersal behaviour and the stiffness of the pavement, while the other fatigable welds are only susceptible to the effect of the stiffness of the pavement.

(2) Based on the effective notch stress approach, the initiation position of root-deck crack varies with the pavement temperature, while it is not affected by the transverse position of wheel load.

(3) The numerical results demonstrate the positive effect of the stress dispersal behaviour through pavement surfac-

Table 3 Comparison of fatigue damages in a year

Loading mode	Mode I			Mode II		
Calculating types	Type A	Type B	Type C	Type A	Type B	Type C
Fatigue damage ($\times 10^{-5}$)	10.2877	46.3981	11.0176	14.4768	67.7681	13.1322

Type A referred to the effective notch stress-based fatigue damage considering the variation of stress concentration position; Type B referred to the effective notch stress-based fatigue damage neglecting the variation of stress concentration position; Type C referred to the fatigue damage evaluated by the equivalent stress at weld root

ing on fatigue durability of rib-to-deck welds, which helps to further improve the fatigue performance of OSDs.

(4) In the process of effective notch stress-based fatigue damage evaluation, the differences in stress concentration positions induced by the variation of ambient temperatures should be reasonably considered.

Compliance with Ethical Standards

Conflict of interest The authors declare that they have no conflict of interest.

References

Aung, M. P., & Hirohata, M. (2019). Numerical study on post weld heat treatment of non-stiffened welded box section member and its compressive behavior. *International Journal of Steel Structures, 19*(5), 1521–1533.

Choi, J. H., & Kim, D. H. (2008). Stress characteristics and fatigue crack behaviour of the longitudinal rib-to-cross beam joints in an orthotropic steel deck. *Advances in Structural Engineering, 11*(2), 189–198.

Cui, C., Zhang, Q. H., Hao, H., Li, J., & Bu, Y. Z. (2018). Influence of asphalt pavement conditions on fatigue damage of orthotropic steel decks: parametric analysis. *Journal of Bridge Engineering, 23*(12), 04018093.

Dong, K. S., Le, V. A., Kim, K. (2013). In-plane ultimate compressive strengths of HPS deck panel system stiffened with U-shaped ribs. *Thin-Walled Structures*, *63*, 70–81.

Fu, Z. Q., Ji, B. H., Ye, Z., & Wang, Y. X. (2017a). Fatigue evaluation of cable-stayed bridge steel deck based on predicted traffic flow growth. *KSCE Journal of Civil Engineering, 21*(4), 1400–1409.

Fu, Z. Q., Wang, Q. D., Ji, B. H., & Yuanzhou, Z. Y. (2017b). Rewelding repair effects on fatigue cracks in steel bridge deck welds. *Journal of Performance of Constructed Facilities, 31*(6), 04017094.

Guo, T., Li, A. Q., & Wang, H. (2008). Influence of ambient temperature on the fatigue damage of welded bridge decks. *International Journal of Fatigue, 30*(6), 1092–1102.

Hobbacher, A. (2015). *Recommendations for fatigue design of welded joints and components*. Berlin: Springer.

Ji, B. H., Liu, R., Chen, C., Maeno, H., & Chen, X. F. (2013). Evaluation on root-deck fatigue of orthotropic steel bridge deck. *Journal of Constructional Steel Research, 90*(5), 174–183.

JTG D64-2015. (2015). *Specifications for design of highway steel bridge*. Beijing: China Communications Press. **(In Chinese)**.

Kainuma, S., Jeong, Y. S., Yang, M. Y., & Inokuchi, S. (2016). Welding residual stress in roots between deck plate and U-rib in orthotropic steel decks. *Measurement, 92,* 475–482.

Kloos, M., & Wall, R. S. (2019). Finite element modelling of the structural behaviour of a novel cellular beam non composite steel structure in fire. *International Journal of Steel Structures, 19*(5), 1367–1380.

Lazzarin, P., & Livieri, P. (2001). Notch stress intensity factors and fatigue strength of aluminum and steel welded joints. *International Journal of Fatigue, 23*(3), 225–232.

Li, M., Hashimoto, K., & Sugiura, K. (2014). Influence of asphalt surfacing on fatigue evaluation of rib-to-deck joints in orthotropic steel bridge decks. *Journal of Bridge Engineering, 19*(10), 04014038.

Li, M., Suzuki, Y., Wang, H. C., Aoki, Y., Adachi, Y., & Sugiura, K. (2016). Experimental study of asphalt surfacing influence on rib-to-deck joints considering temperature and dynamic effects. *Journal of Bridge Engineering, 21*(11), 04016077.

Liu, R., Wang, B., & Liu, Y. Q. (2015). Distortion induced fatigue of deck plate at rib intersection with diaphragm in orthotropic steel deck. *International Journal of Steel Structures, 15*(3), 623–632.

Liu, Y., Qian, Z. D., & Hu, H. Z. (2016a). Thermal field characteristic analysis of steel bridge deck during high-temperature asphalt pavement paving. *KSCE Journal of Civil Engineering, 20*(7), 2811–2821.

Liu, Y., Zhang, H. P., Liu, Y. M., Deng, Y., Jiang, N., & Lu, N. W. (2016b). Fatigue reliability assessment for orthotropic steel deck details under traffic flow and temperature loading. *Engineering Failure Analysis, 71,* 179–194.

Oh, D. J., Lee, J. M., & Kim, M. H. (2014). Fatigue strength assessment of Invar alloy weld joints using the notch stress approach. *Engineering Failure Analysis, 42*(5), 87–99.

Pedersen, M. M., Mouritsen, O. Ø., Hansen, M. R., Andersen, J. G., & Wenderby, J. (2010). Re-analysis of fatigue data for welded joints using the notch stress approach. *International Journal of Fatigue, 32*(10), 1620–1626.

Rahnavard, R., & Thomas, R. J. (2018). Numerical evaluation of the effects of fire on steel connections; Part 1: Simulation techniques. *Case Studies in Thermal Engineering, 12,* 445–453.

Rahnavard, R., & Thomas, R. J. (2019). Numerical evaluation of the effects of fire on steel connections; Part 2: Model results. *Case Studies in Thermal Engineering, 13,* 100361.

Wang, Q. D., Ji, B. H., Fu, Z. Q., & Ye, Z. (2019). Evaluation of crack propagation and fatigue strength of rib-to-deck welds based on effective notch stress method. *Construction and Building Materials, 201,* 51–61.

Xiao, Z. G., Yamada, K., Inoue, J., & Yamaguchi, K. (2005). Fatigue cracks in longitudinal ribs of steel orthotropic deck. *International Journal of Fatigue, 28*(4), 409–416.

Xiao, Z. G., Yamada, K., Ya, S., & Zhao, X. L. (2008). Stress analyses and fatigue evaluation of rib-to-deck joints in steel orthotropic decks. *International Journal of Fatigue, 30*(8), 1387–1397.

Ya, S., Yamada, K., & Shikawa, T. (2011). Fatigue evaluation of rib-to-deck welded joints of orthotropic steel bridge deck. *Journal of Bridge Engineering, 18*(5), 492–499.

Yan, F., Chen, W. Z., & Lin, Z. B. (2016). Prediction of fatigue life of welded details in cable-stayed orthotropic steel deck bridges. *Engineering Structures, 127,* 344–358.

Zhang, Q. H., Cui, C., Bu, Y. Z., Liu, Y. M., & Ye, H. W. (2015). Fatigue tests and fatigue assessment approaches for rib-to-diaphragm in steel orthotropic decks. *Journal of Constructional Steel Research, 114,* 110–118.

Publisher's Note Springer Nature remains neutral with regard to jurisdictional claims in published maps and institutional affiliations.